MATERIALS SCIENCE

# Anti-twinning in nanoscale tungsten

**Jiangwei Wang[1]*, Zhi Zeng[2], Minru Wen[2,3], Qiannan Wang[1], Dengke Chen[2], Yin Zhang[2], Peng Wang[4,5], Hongtao Wang[4], Ze Zhang[1], Scott X. Mao[6], Ting Zhu[2]***



**Nanomaterials often surprise us with unexpected phenomena. Here, we report a discovery of the anti-twinning deformation, previously thought impossible, in nanoscale body-centered cubic (BCC) tungsten crystals. By conducting in situ transmission electron microscopy nanomechanical testing, we observed the nucleation and growth of anti-twins in tungsten nanowires with diameters less than about 20 nm. During anti-twinning, a shear displacement of 1/3⟨111⟩ occurs on every successive {112} plane, in contrast to an opposite shear displacement of 1/6⟨$\bar{1}\bar{1}\bar{1}$⟩ by ordinary twinning. This asymmetry in the atomic-scale shear pathway leads to a much higher resistance to anti-twinning than ordinary twinning. However, anti-twinning can become active in nanosized BCC crystals under ultrahigh stresses, due to the limited number of plastic shear carriers in small crystal volumes. Our finding of the anti-twinning phenomenon has implications for harnessing unconventional deformation mechanisms to achieve high mechanical preformation by nanomaterials.**

## INTRODUCTION

Nanoscale body-centered cubic (BCC) transition metals hold great promise for applications in microelectromechanical devices under extreme loading conditions. Given the general tendency of smaller being stronger, they are expected to outperform bulk BCC counterparts that have excellent mechanical properties over a wide range of temperatures. However, the mechanical behavior of nanoscale BCC metals remains much less understood compared to nanoscale face-centered cubic (FCC) metals (*1*). It is partly due to the complex deformation characteristics of BCC crystals (*2*–*4*) that are usually associated with the unique nonplanar core structure of screw dislocations (*2*, *5*–*8*). It is also partly due to a strong competition between dislocation slip and deformation twinning under the prevailing ultrahigh stresses in nanosized volumes. To understand this competition, it is essential to clarify various dislocation and twinning modes in BCC crystals, including the asymmetric twinning and anti-twinning. That is, on the {112} twin plane, the resistance to ordinary twinning with a forward shear along ⟨111⟩ is markedly lower than that to anti-twinning through a reverse shear along ⟨$\bar{1}\bar{1}\bar{1}$⟩ (*2*, *9*–*12*). This asymmetry arises because of different atomic arrangements in the two opposite shear pathways along ⟨111⟩ and ⟨$\bar{1}\bar{1}\bar{1}$⟩ on the {112} twin plane (*2*, *3*). Given the high resistance encountered (*2*, *9*–*12*), anti-twinning had been deemed impossible. This is because plastic shear can be favorably produced by dislocation slip and/or ordinary twinning that is driven by lower shear stresses but experiences much lower resistances compared to anti-twinning (*2*, *3*). To our knowledge, there is no report on experimental observations of anti-twinning in BCC crystals to date.

Generally speaking, plastically deforming BCC nanocrystals are prone to a rapid loss of dislocations from their free surfaces, leading to dislocation starvation (*13*–*15*). To maintain continued plastic deformation, high stresses are applied to activate the nucleation of dislocations and even deformation twins from the surfaces and interfaces (if present) of BCC nanocrystals (*16*). As a result, deformation twinning, which usually occurs at low temperatures and high strain rates in bulk samples (*16*–*18*), often becomes active in BCC nanocrystals at room temperature and low strain rates (*16*, *19*, *20*). However, the existing experimental and theoretical studies have been mostly focused on ordinary twinning in BCC metallic nanocrystals (*16*, *21*, *22*), as summarized in tables S1 and S2. Whether anti-twinning can occur in these BCC nanocrystals remains unclear (*14*–*16*). If happened, it is essential to determine the critical sample size below which anti-twinning becomes favored.

Here, we report direct observations of anti-twinning in BCC tungsten (W) nanowires by conducting in situ transmission electron microscopy (TEM) nanomechanical testing. With the decrease of nanowire diameter, an unexpected anti-twinning phenomenon is observed. This result demonstrates that the nucleation and growth of anti-twins can favorably occur in BCC nanocrystals under ultrahigh stresses. We perform molecular dynamics (MD) simulations and density functional theory (DFT) calculations to provide mechanistic insights into the nucleation and growth processes of anti-twins. Our findings not only advance the understanding of size-dependent deformation in BCC nanocrystals but also suggest a possibility of harnessing unconventional deformation mechanisms to achieve high mechanical preformation in nanomaterials.

## RESULTS

### Twinning versus anti-twinning in [$\bar{1}$10]-oriented W nanowires

Figures 1 (A and B) shows the schematic illustrations of the crystallographic origin of twinning and anti-twinning asymmetry in a [$\bar{1}$10]-oriented BCC single crystal under axial loading. When a BCC crystal is viewed along the [110] direction, the ($\bar{1}\bar{1}$2) twin plane becomes edge on. The squares and circles in Fig. 1 (A and B) represent atoms in the alternating ($\bar{1}\bar{1}$2) atomic planes along the viewing direction of [110]. The stacking sequence of ($\bar{1}\bar{1}$2) atomic planes is marked by ABCDEF and also indicated by dashed lines. Under ⟨110⟩ tension, the direction of the resolved shear stress on the {112} plane dictates that only anti-twinning can occur, but not ordinary twinning, because the resistance to the latter is much higher than the former. When anti-twinning occurs, it should produce a shear

[1]Center of Electron Microscopy and State Key Laboratory of Silicon Materials, School of Materials Science and Engineering, Zhejiang University, Hangzhou 310027, China. [2]Woodruff School of Mechanical Engineering, Georgia Institute of Technology, Atlanta, GA 30332, USA. [3]School of Physics and Optoelectronic Engineering, Guangdong University of Technology, Guangzhou 510006, China. [4]Center for X-Mechanics, Zhejiang University, Hangzhou 310027, China. [5]Materials Genome Institute, Shanghai University, Shanghai 200444, China. [6]Department of Mechanical Engineering and Materials Science, University of Pittsburgh, Pittsburgh, PA 15261, USA.
*Corresponding author. Email: jiangwei_wang@zju.edu.cn (J.W.); ting.zhu@me.gatech.edu (T.Z.)

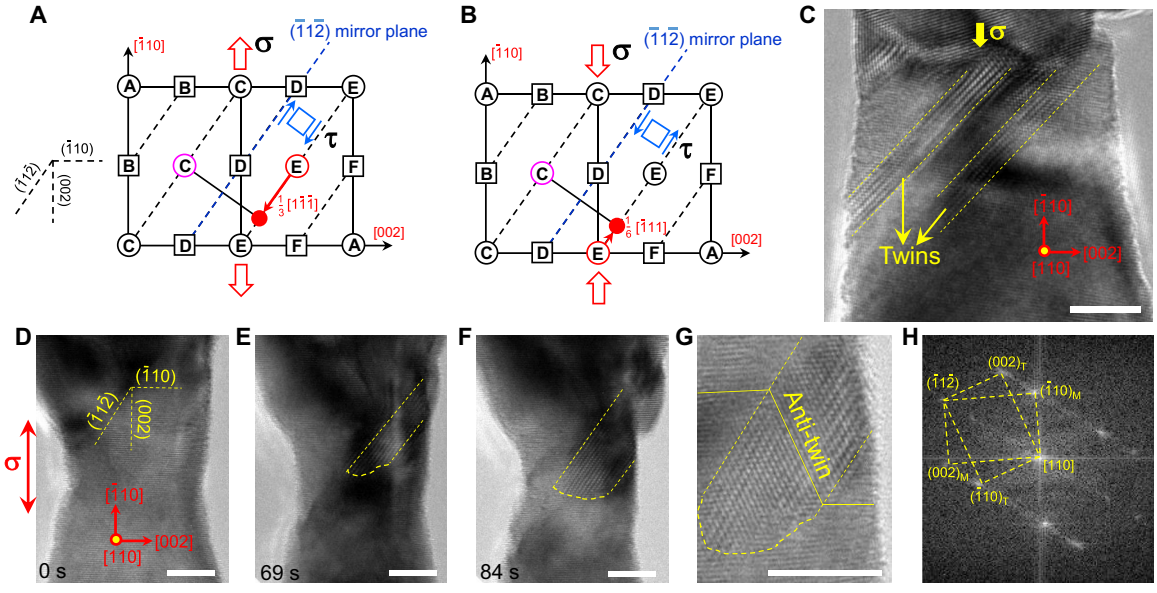


**Fig. 1. Twinning versus anti-twinning in [1̄10]-oriented W nanowires.** (**A** and **B**) Schematic illustration of the crystallographic origin of twinning and anti-twinning asymmetry in a [1̄10]-oriented BCC crystal under axial loading. The squares and circles represent the atoms in the alternating (1̄12̄) planes along the [110] viewing direction. The red arrow in (A) and pink arrow in (B) represent the shear displacement vector of twinning and anti-twinning, respectively. (**C**) TEM image showing the deformation-induced ordinary twinning via 1/6[1̄11](1̄12̄) shear in a W bicrystal nanowire (~18 nm in diameter) under [1̄10] compression. (**D** to **F**) TEM images showing the deformation-induced anti-twinning in a W bicrystal nanowire (~16 nm in diameter) under [1̄10] tension. The sample was loaded at a strain rate of $10^{-3}$ $s^{-1}$. The anti-twin embryo first nucleated from the side surface and then grew into the crystal by expanding its leading edge and thickening the anti-twin band. (**G** and **H**) Magnified TEM image and fast Fourier transform pattern of the anti-twin. Scale bars, 5 nm.

displacement of 1/3⟨111⟩ on every successive {112} twin plane; this response is dictated by the lattice geometry of the BCC structure, as illustrated in Fig. 1A. More specifically, Fig. 1A shows that under [1̄10] tension, the resolved shear stress τ on the (1̄12̄) plane (as marked on a square stress element) will move the atomic layer E relative to the atomic layer D in the direction of [1 1̄ 1̄] (marked by the red arrow), but not in the opposite direction. When anti-twinning occurs, the atom E that is marked by a red hollow circle should move by 1/3[1 1̄ 1̄] to the site indicated by a red solid circle so that it becomes a mirror reflection of the atom C that is marked by a pink hollow circle. A similar analysis can be applied to the case of ordinary twinning by a shear displacement of 1/6[1̄11] under [1̄10] compression, as shown in Fig. 1B. The different amounts of shear displacement for anti-twinning and twinning are dictated by the mirror symmetry requirement between the displaced atom E and fixed atom C with respect to the mirror twin plane. Moreover, during anti-twinning (Fig. 1A), the atomic layer D is located under the shear displacement path of the atomic layer E and thus imposes a strong resistance to the anti-twinning shear. However, this is not the case for ordinary twinning (Fig. 1B). As a result, the resistance to anti-twinning should be much higher than that of ordinary twinning (*2*, *9*–*12*), causing a lower possibility of anti-twinning in BCC crystals (*6*, *14*, *15*).

To conduct in situ TEM nanomechanical tests of W nanocrystals, we used a recently developed in situ nanowelding method (*16*) to fabricate individual W bicrystal nanowires containing a cross-sectional grain boundary (Materials and Methods). This method overcomes the difficulties of other nanofabrication methods such as focused ion beam machining in producing a stable sub–100-nm BCC sample without damage and contamination (*16*). Figure 1C and fig. S1 show the in situ TEM observations of ordinary twinning along 1/6[1̄11](1̄12̄) in a W bicrystal nanowire (~18 nm in diameter) under [1̄10] compression. This twinning mode is consistent with the schematic illustration in Fig. 1B and becomes active under the largest resolved shear stress among all the possible twinning systems (*16*) (see the respective Schmid factors listed in Table 1). Note that the bicrystal sample is referred to as a [1̄10]-oriented nanowire, because the plastic deformation events of interest are primarily observed in the relatively large crystal with its [1̄10] axis along the loading direction. In contrast, Fig. 1 (D to F) shows the in situ TEM observations of anti-twinning along 1/3[1 1̄ 1̄](1̄12̄) in a W bicrystal nanowire (~16 nm in diameter) under [1̄10] tension. Under an applied strain rate of ~$10^{-3}$ $s^{-1}$, an anti-twin embryo first nucleated from the side surface of the nanowire (Fig. 1E). Then, this anti-twin embryo grew into the nanowire by expanding its leading edge and increasing its thickness via successive nucleation of anti-twin partials on the (1̄12̄) twin boundaries (Fig. 1, E and F). The magnified TEM image in Fig. 1G and fast Fourier transform pattern in Fig. 1H confirm the occurrence of anti-twinning. We emphasize that the partial dislocation on the anti-twin boundary has a larger Burgers vector of 1/3[1 1̄ 1̄] on the (1̄12̄) twin plane compared with the partial dislocation on the ordinary twin boundary with a smaller Burgers vector of 1/6[1̄11] (*22*); this difference is dictated by the crystallography of the BCC lattice.

In addition to the surface nucleation of anti-twins, we observed an anti-twin nucleated near a grain boundary inside a bicrystal W nanowire under [1̄10] tension (Fig. 2A). In this case, a [1̄1̄](1̄12) anti-twin with a very thin leading edge (less than ~1 nm) was emitted from the grain boundary (Fig. 2B) under an ultrahigh tensile stress of ~26.2 GPa (fig. S2). The formation of such an anti-twin resulted in the release of lattice strain and thus tensile stress in the nanowire (fig. S3). Associated with this process was the slow growth of this

**Table 1. Schmid factors for different deformation modes in BCC W nanowires under [$\bar{1}$10] compression (C) and tension (T).**

| Loading modes | Dislocations | | Twins | | Deformation modes |
|---|---|---|---|---|---|
| | Slip systems | Schmid factors | Twin systems | Schmid factors | |
| C | 1/2[1$\bar{1}$1]($\bar{1}$01)<br>1/2[$\bar{1}$11](101)<br>1/2[1$\bar{1}$1](011)<br>1/2[$\bar{1}$11]($0\bar{1}$1) | 0.41 | 1/6[$\bar{1}$11]($\bar{1}$1$\bar{2}$)<br>1/6[1$\bar{1}$1]($\bar{1}$12) | 0.47 | Twinning |
| T | 1/2[1$\bar{1}$1]($\bar{1}$01)<br>1/2[$\bar{1}$11](101)<br>1/2[1$\bar{1}$1](011)<br>1/2[$\bar{1}$11]($0\bar{1}$1) | 0.41 | 1/3[1$\bar{1}\bar{1}$]($\bar{1}$1$\bar{2}$)<br>1/3[$\bar{1}\bar{1}$1]($\bar{1}$12) | 0.47 | Anti-twinning |

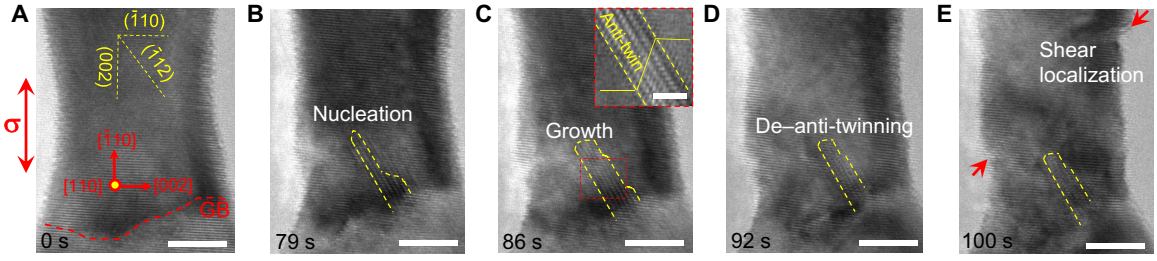


**Fig. 2. In situ TEM observation of a dynamic anti-twinning process in a bicrystal W nanowire under [$\bar{1}$10] tension.** (**A**) Pristine bicrystal W nanowire with a cross-sectional grain boundary (GB). (**B**) An anti-twin with a very thin leading edge (less than ~1 nm) was emitted from the grain boundary. (**C** and **D**) The anti-twin grew slowly into the crystal (C) until de–anti-twinning occurred, resulting in anti-twin shrinkage (D). Inset in (C) shows the structure of this anti-twin. (**E**) Further straining caused a localized shear deformation mediated by the glide of dislocations nucleated from the side surface. Red arrows in (E) indicate the surface steps produced by dislocation slip. Scale bars in (A) to (E) are 5 nm; scale bar in the inset of (C) is 1 nm.

anti-twin (Fig. 2C), which was followed by de–anti-twinning, resulting in anti-twin shrinkage (Fig. 2D). The de–anti-twinning was likely caused by stress release associated with the formation of dislocations, anti-twins, and/or twins at other locations in the nanowire. However, these stress-releasing processes were not captured by TEM observations, as their crystallographic orientations might not be aligned favorably with the specific ⟨110⟩ zone axis taken for anti-twin imaging. As the applied tensile load was further increased, a localized shear deformation, which was mediated by dislocation activities, occurred near the side surface of the nanowire (Fig. 2E). The above in situ TEM results indicate that anti-twinning in W nanowires faces a strong competition from dislocation slip. This competition can take place during anti-twin nucleation and growth, indicative of high energy barriers for anti-twinning shear. Among the four tungsten nanowires (with the diameter less than 20 nm) tested under [110] tension, we observed the anti-twinning deformation in three samples (another bicrystal sample fractured from its weak grain boundary, and thus, no anti-twinning occurred). Similar anti-twinning deformation was also observed in a W nanowire under [111] tension (fig. S4) and in other BCC metals such as a Nb nanowire under [112] tension (fig. S5); note that [111] tension and [112] tension are anti-twinning orientations for BCC metals (table S1). These in situ TEM experiments suggest that anti-twinning in BCC metallic nanowires can occur with a reasonably high frequency, establishing the anti-twinning shear as a viable plastic deformation mode in BCC metallic nanocrystals. We note that the shear displacement caused by an anti-twinning dislocation cannot be directly identified in our experiments due to the TEM resolution limit, especially under in situ loading, but can be clearly revealed by atomistic simulations as shown next.

## Atomistic modeling of anti-twinning

To understand the dynamic process of anti-twinning, MD simulations with a Finnis-Sinclair–type potential of W by Ackland and Thetford (*23*) were performed for a single-crystal W nanowire under [$\bar{1}$10] tension (Materials and Methods). Figure 3A shows the simulated stress-strain curve, while Fig. 3 (B and C) shows the overall nanowire structure right before and at the end of a major stress drop in the stress-strain curve. It is seen that anti-twinning occurred during this stress drop (Fig. 3, A to C), consistent with the experimental observations (Fig. 2 and fig. S3). The MD snapshots in Fig. 3 (D to G) show the nucleation and growth of an anti-twin from the nanowire surface, as indicated by the blue lines that become kinked because of the anti-twinning. More specifically, an anti-twin embryo first nucleated from the side surface and then grew through the nanowire (Fig. 3, D to G). The growth of the anti-twin involved both expansion of its leading edge (Fig. 3, E and F) and lateral movement of the ($\bar{1}$1$\bar{2}$) twin boundary, resulting in the formation of an anti-twin band (Fig. 3G). Close examination indicates that the anti-twin growth was mediated by the surface nucleation and glide of 1/3[1$\bar{1}\bar{1}$]($\bar{1}$1$\bar{2}$) dislocations on the boundary between the growing anti-twin and its parent crystal. The core of a 1/3[1$\bar{1}\bar{1}$]($\bar{1}$1$\bar{2}$) anti-twin dislocation is highlighted by a pink circle in Fig. 3H, where a large shear displacement in the core causes a marked separation between the two adjacent {112} atomic layers in the core, as seen by relatively large interstices enclosed by the blue atoms in the core. The core of this anti-twin boundary dislocation coincides with an anti-twin boundary step, as marked by the stepped red line in Fig. 3H. Hence, the coincident dislocation and step at the anti-twin boundary constitute a so-called disconnection (*24*), which is reminiscent of the coincident dislocation and step, i.e., a disconnection, at the boundary of an ordinary twin. This process of surface nucleation and

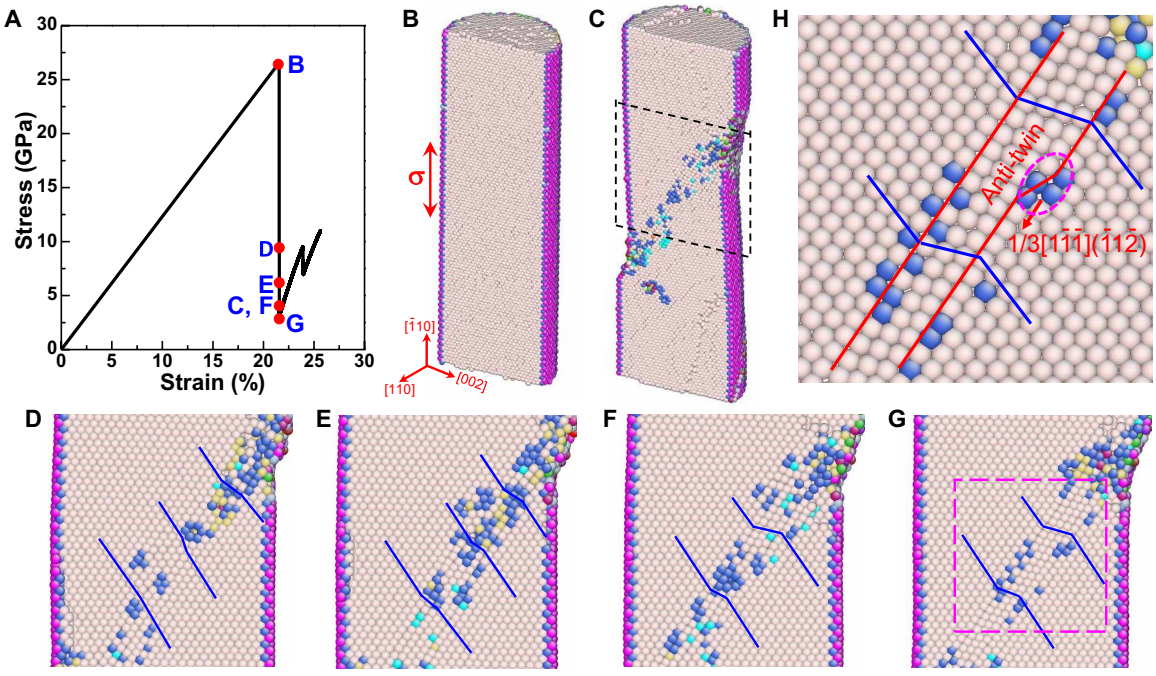


**Fig. 3. MD simulation of anti-twinning in a W nanowire under [1̄10] tension.** (**A**) MD-simulated tensile stress-strain curve. (**B** and **C**) Simulated nanowire structure right before and at the end of the major stress drop, with the corresponding tensile stresses marked by the red dots in (A). (**D** to **G**) Local atomic structures [corresponding to the boxed region in (C)] showing the nucleation and growth of an anti-twin from the nanowire surface. Blue lines are drawn along the close-packed ⟨111⟩ direction, showing the perfect and twinned BCC lattice. The corresponding tensile stress for each structure is marked by the red dot in (A). (**H**) Local atomic structure [corresponding to the squared region in (G)], showing the 1/3[1$\bar{1}\bar{1}$](1$\bar{1}\bar{2}$) dislocation at the boundary of an anti-twin. The core of this anti-twin boundary dislocation (marked by the pink circle) coincides with an anti-twin boundary step (marked by the stepped red line). Atoms in (B) to (H) are color-coded by the coordination numbers.

growth of an anti-twin from MD is similar to that from in situ TEM observations (Fig. 1) but reveals the atomic-level details of glide of anti-twin boundary dislocations. In addition, we note that during MD simulations, surface nucleation and glide of dislocations in the nanowire lattice occurred before anti-twinning (fig. S6). However, most dislocations escaped from the nanowire surface, while the rest trapped each other inside the nanowire, making it difficult for continued dislocation nucleation and glide. Because the overall plastic strain produced by these dislocation activities was insufficient to match the applied tensile strain, a large elastic strain was induced. This led to the buildup of high stresses for triggering the anti-twinning shear in MD simulations. Similar dislocation processes might also occur before anti-twinning during experiment. However, they were not captured by in situ TEM observations shown in Fig. 1, due to the fast processes of dislocation nucleation and glide. MD simulations were also performed using an embedded atom method (EAM) potential of W developed by Marinica *et al.* (*25*), and similar dislocation and anti-twin activities were observed, as shown in fig. S7.

To further understand the competition between anti-twinning and ordinary twinning, we performed DFT calculations (*4*) to determine the energy landscapes of multilayer anti-twinning shear and ordinary twinning shear in BCC W single crystals. As illustrated in Fig. 4A, the energy landscape curve of anti-twinning and ordinary twinning was respectively calculated by successively moving one {112} atomic layer with respect to a previously moved one by $2b_p$ and $b_p$, where $b_p$ is the Burgers vector length of a 1/6⟨111⟩ twin partial. As a result, the thickness of anti-twin and ordinary twin increases by one {112} atomic layer, respectively. The energy landscape

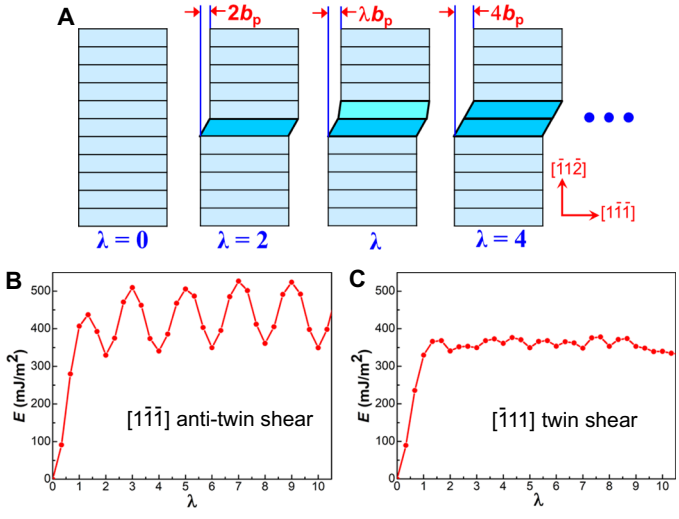


**Fig. 4. DFT results of the energy landscapes of anti-twinning shear and ordinary twinning shear in BCC W.** (**A**) Schematic illustration of DFT calculation of anti-twinning by successive shearing of one (1$\bar{1}\bar{2}$) atomic layer with respect to a previously moved one in the [1$\bar{1}\bar{1}$] direction by $\lambda b_p$, where $b_p$ is the Burgers vector length of a 1/6⟨111⟩ twin partial. Ordinary twinning involves shearing in the [1̄11] direction by $\lambda b_p$. (**B**) Energy landscape curve of anti-twinning shear, showing a series of local energy minima (when λ is an even number), each of which corresponds to an anti-twin band with a different number of atomic layers. (**C**) Energy landscape curve of ordinary twinning shear, showing a series of local energy minima (when λ is an integer), each of which corresponds to an ordinary twin band with a different number of atomic layers.

curve of multilayer anti-twinning exhibits a series of local energy minima (Fig. 4B), each of which corresponds to an anti-twin band with a different number of atomic layers. A local energy maximum exists between two adjacent local energy minimum states, indicating a finite energy barrier (~0.163 J/m$^2$) for anti-twin thickening (Fig. 4B). In contrast, the energy landscape curve of multilayer ordinary twinning exhibits much lower energy barriers to twin thickening (Fig. 4C). Hence, these DFT results indicate that the nucleation and growth of an anti-twin band are more difficult than an ordinary twin, due to the higher energy barrier of the former (Fig. 4B). As a result, anti-twinning is less favored than ordinary twinning in bulk BCC crystals, while the ultrahigh stresses in nanosized BCC crystals facilitate the dynamic competition among anti-twinning, ordinary twinning, and dislocation slip, as demonstrated by the in situ TEM observations in Fig. 2. It should be noted that the stability of an anti-twin in a mechanically loaded W nanowire is controlled not only by the energy of anti-twinning shear layer by layer but also by several other competing factors, including the anti-twin boundary energy, elastic energy in the surrounding matrix, and mechanical work associated with the applied load.

### Size-dependent anti-twinning in [$\bar{1}$10]-oriented W nanowires

Our in situ TEM experiments further revealed the size-dependent response of anti-twinning in BCC W nanowires under [$\bar{1}$10] tension. From a series of in situ experiments of W nanowires with different diameters, we found that anti-twinning frequently occurred in small-diameter W nanowires, but dislocation slip predominated the plastic shear with increasing nanowire diameter. Figure 5 shows an example of dislocation-dominated deformation in a large W nanowire (~45 nm in diameter) under [$\bar{1}$10] tension, as confirmed in Fig. 5 (A to C). Before the tensile loading, no preexisting dislocation was observed in the nanowire (Fig. 5, A and C). Upon tensile loading, a half-dislocation loop with the Burgers vector of 1/2⟨111⟩{110} was nucleated from the free surface and then expanded into the nanowire (Fig. 5D). This process is similar to the surface dislocation nucleation observed in other BCC nanowires (*13*). We note that the surface intersection point of the expanding dislocation loop (marked by the blue arrows in Fig. 5, E and F) could act as an effective pinning point for dragging dislocation motion, causing slow rotation of the dislocation line around the pinning point. Incidentally, this dragging effect of the surface intersection point may induce the self-multiplication of dislocation inside BCC nanocrystals, as suggested by previous MD simulations (*8*), while this self-multiplication was not observed during our in situ experiment. Further straining of the nanowire caused the escape of dislocations from the surface during in situ experiment, leading to dislocation starvation in the small-volume nanowire (Fig. 5G). Subsequently, new surface dislocations were seen to nucleate and grow for continued plastic deformation (Fig. 5, H to K). These results demonstrate the dislocation-mediated plasticity in large W nanocrystals (*14*). The continued, but limited, dislocation activities finally led to the necking (Fig. 5K) and fracture of the W nanowire.

## DISCUSSION

The anti-twinning deformation in BCC crystals (*2*, *3*) had been deemed impossible, given the intrinsically high resistance to anti-twinning shear. Dislocation slip and/or ordinary twinning shear usually predominate the plastic deformation of bulk and small-volume BCC crystals, even when anti-twinning shear is favored (see table S2). By taking advantage of a recently developed capability of in situ fabrication of sub–20-nm W nanowires, our in situ TEM nanomechanical testing revealed an anti-twinning phenomenon and further demonstrated a size dependence of anti-twinning deformation in BCC metallic nanowires (Figs. 1 and 2 and figs. S4 and S5).

The size dependence of anti-twinning deformation mainly originates from the size-strengthening effect, as well as the competing operation between ordinary dislocation and anti-twin in nanoscale W crystals. Typically, the smaller the nanowire, the higher the strength (*1*). Given the high nucleation barrier of an anti-twin, the deformation of W nanowires with large sizes (e.g., 45 nm) was dominated by dislocations that are favored at relatively low stresses. However, the nucleation stress of dislocations increased markedly with decreasing nanowire diameter (*16*), which may become comparable to the nucleation stress of an anti-twin at the sub–20-nm scale. As a result, anti-twinning can become a favored deformation mode in W nanowires with sizes less than 20 nm. But anti-twinning still has to compete with other familiar modes of plastic shear, given the relatively close Schmid factors for ordinary dislocation (0.41) and anti-twinning dislocation (0.47), as well as the high stresses applied. Our MD simulations revealed the surface nucleation of ordinary dislocations before anti-twinning (fig. S6). Hence, it is necessary to analyze how the prevalent ultrahigh stresses in nanosized W crystals dictate the competition of the nucleation-controlled plastic shear by dislocations, twins, and anti-twins (*16*). For the W nanowires under [$\bar{1}$10] compression, the theoretical shear stress (at 0 K) for dislocation slip on its most favored {110} plane and ordinary twinning shear on its most favored {112} plane are comparable (~18 GPa) (*16*) such that the competition between these two plastic shear modes becomes possible (*16*, *26*). In contrast, under [$\bar{1}$10] tension, the theoretical shear stress for anti-twinning on its most favored {112} plane is ~25 GPa (*26*, *27*), which is markedly higher than that for dislocation slip and ordinary twinning shear (~18 GPa) (*16*). However, the larger normal stress on the most favored {112} plane for anti-twinning shear could reduce its resistance to some extent (*27*, *28*), favoring the competition of anti-twinning over dislocation slip. In this work, the measured tensile "yield" stress is ~26.2 GPa (fig. S2B) when anti-twinning was observed in the 16-nm-diameter W nanowire under [$\bar{1}$10] tension. The corresponding resolved shear stress is ~12.3 GPa on the most favored {112} twin plane for driving anti-twinning shear. The experimentally measured tensile stress is lower than the aforementioned theoretical value (at 0 K) for anti-twinning. This difference can be attributed to the effects of free surface (including surface defects) and room temperature on reducing the critical shear stress of anti-twinning. It is known that the free surface has important influences on defect dynamics in nanosized crystals (*1*, *16*). Surface dislocation nucleation can cause local structural changes at the nucleation site such that it cannot occur continuously at the same surface site. In contrast, once an anti-twin nucleates, this anti-twin could continue its growth process more easily by nucleation of an anti-twin dislocation from the intersection between the anti-twin boundary and free surface; due to the migration of the anti-twin boundary, this intersection is not fixed in space, thus reducing the impact of structural changes at a particular nucleation site so as to favor the continued anti-twinning process. However, with an increasing diameter and thus surface area of the nanowire, the amount of surface heterogeneities rises. These surface heterogeneities could

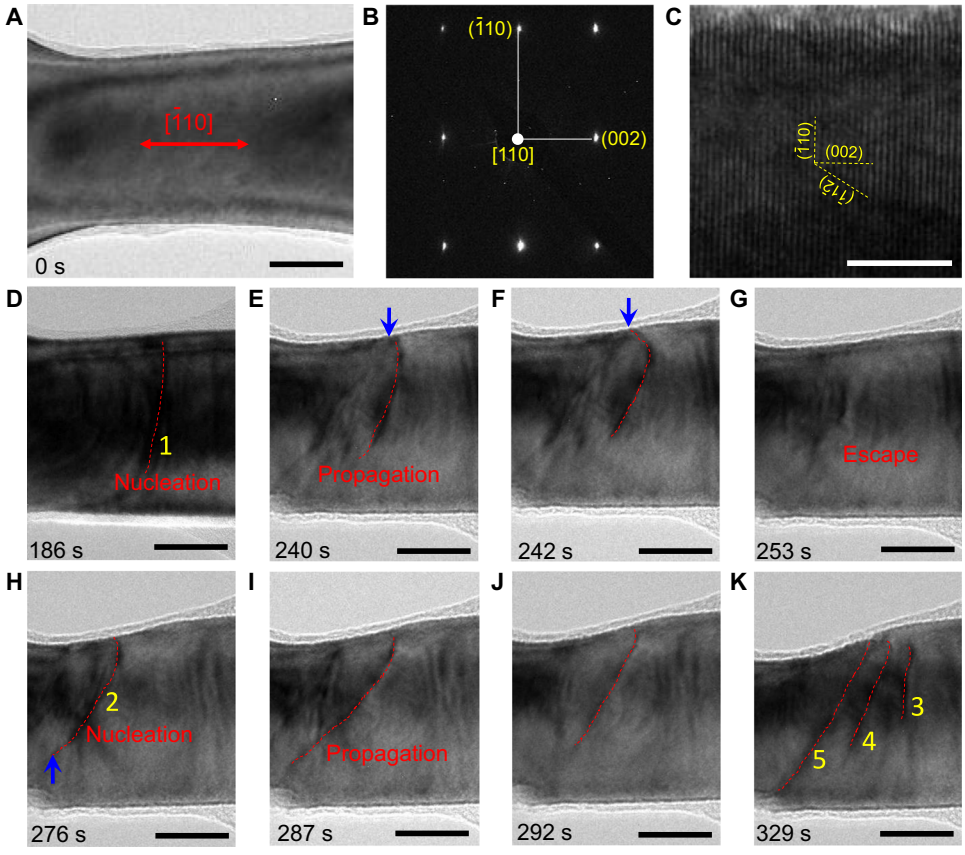


**Fig. 5. Dislocation-dominated plasticity in a 45-nm W nanowire under [1̄10] tension.** (**A**) TEM image of the [1̄10]-oriented nanowire with a diameter of 45 nm and without preexisting dislocations. (**B**) Selected area electron diffraction pattern and (**C**) high-magnification TEM image showing the axial orientation [1̄10] of the nanowire. (**D** to **K**) TEM images showing the dynamic dislocation process in the nanowire. Under tensile loading, a half-dislocation loop with the Burgers vector of 1/2⟨111⟩{110} was emitted from the surface and propagated into the nanowire (D); further loading causes the rotation of the dislocation line around the surface pinning point (E and F); the dislocation escaped from the surface of the nanowire (G); the nucleation of new dislocations for continued plastic deformation (H to K). The surface intersection points of dislocations are marked by the blue arrows in (E), (F), and (H). Scale bars in (A) and (D) to (K) are 20 nm; scale bar in (C) is 5 nm.

favor dislocation nucleation, leading to a transition from anti-twinning shear to dislocation slip, as observed from BCC W nanowires (Figs. 1 and 4) and Nb nanowires (fig. S5). This transition could be partly attributed to the sluggish growth of anti-twins due to the high energy barriers for anti-twinning shear (Fig. 4B), as well as by the occurrence of large stress drop after anti-twin nucleation (fig. S3). Hence, the dynamic transitions among anti-twinning, de–anti-twinning, and dislocation slip became possible, as revealed in Fig. 2. Although this work has revealed a size-dependent transition between dislocation slip and anti-twinning shear in BCC metallic nanowires, the critical size of anti-twin formation in W nanowires cannot be quantitatively determined because of technical challenges that limit the number of samples tested. Moreover, the impact of crystal orientations and loading conditions (such as high strain rates and low temperatures) on the activation of anti-twinning warrants further study in the future to gain a comprehensive understanding of the anti-twinning phenomenon in BCC nanocrystals. We also note that due to the complexity of surface structure, a systematic understanding of the surface effects on competition between twinning, anti-twinning, and ordinary dislocation slip requires further experiments and simulations in the future.

In conclusion, we have found an anti-twinning phenomenon in BCC W nanowires with diameters less than ~20 nm. A transition from dislocation slip to anti-twinning shear with deceasing nanowire diameter was observed and attributed to the limited plastic deformation carriers in nanosized BCC crystals. The resultant ultrahigh stresses trigger the formation and growth of anti-twins. This work sheds new light onto the size-dependent deformation in small-volume BCC crystals and has broad implications for harnessing unconventional deformation mechanisms toward the high mechanical preformation of nanomaterials. Our discovery calls for a rethink of the active deformation mechanisms in nanoscale BCC metals and may also stimulate investigations of size-dependent anomalous deformation behavior (e.g., tension-compression asymmetry and breakdown of Schmid's law) in these materials.

## MATERIALS AND METHODS

### In situ sample fabrication and nanomechanical testing

Tungsten nanowires with different orientations were fabricated by in situ welding of nanocrystals inside an FEI Tecnai F20 field emission gun TEM equipped with a PicoFemto® TEM electrical holder from Zeptools Co. During welding, a W probe was driven by a piezo-controller to contact a nanoscale edge on the fracture surface of another W rod (99.98 wt % purity, 0.010 inches in diameter). The contact was quickly welded together under a preapplied potential of

2 to 4 V, forming a W nanowire with nearly uniform diameter. In situ nanomechanical testing of the W nanowire was performed with a strain rate of $10^{-3}$ $s^{-1}$ at room temperature. The deformation process was recorded by a charge-coupled device camera at three frames per second.

### MD simulation

To study the anti-twinning deformation in a W nanowire under [$\bar{1}$10] tension, MD simulations were performed using the general MD program LAMMPS. The simulated single-crystal W nanowire has an initial length of 26.8 nm and a circular cross section with a diameter of 7.2 nm. The total number of atoms is 98,340. The Finnis-Sinclair–type potential of W by Ackland and Thetford (*23*) was used for MD simulations. The periodic boundary condition was imposed along the axial direction of the nanowire, and the side surface was traction free. A tensile strain rate of $10^{8}$ $s^{-1}$ was applied, while the temperature was kept at 300 K. The time step was taken as 1 fs. MD simulations were also performed using an EAM potential of W developed by Marinica *et al.* (*25*) to further validate the observations from in situ TEM experiments as well as MD simulations using the Ackland-Thetford potential (*23*).

### DFT calculation

To study the energy landscape underlying the multilayer anti-twinning shear and ordinary twinning shear in BCC W, first-principles DFT calculations were performed using the Vienna Ab initio Simulation Package. We built a slab model with 25 layers of W ([$\bar{1}$10]× 1/2[111]× 4[11$\bar{2}$]) and 15 Å vacuum region in the [11$\bar{2}$] direction. The ion electron interaction was described by the projector-augmented wave method (*29*), and the exchange-correlation function was described by the generalized gradient approximation in the parametrization of Perdew-Burke-Ernzerhof (*30*). The plane wave cutoff was set to 300 eV. A 11 × 18 × 1 *k*-point mesh following the Monkhorst-Pack scheme (*31*) was adopted. The energy convergence criterion for the electronic self-consistency was $10^{-5}$ eV. The ionic relaxation was stopped until the maximum force on each atom was less than 0.05 eV/Å.

## SUPPLEMENTARY MATERIALS

Supplementary material for this article is available at http://advances.sciencemag.org/cgi/content/full/6/23/eaay2792/DC1

## REFERENCES AND NOTES


1. T. Zhu, J. Li, Ultra-strength materials. *Prog. Mater. Sci.* **55**, 710–757 (2010).
2. J. W. Christian, Some surprising features of the plastic deformation of body-centered cubic metals and alloys. *Metall. Trans. A.* **14**, 1237–1256 (1983).
3. M. S. Duesbery, V. Vitek, Plastic anisotropy in b.c.c. transition metals. *Acta Mater.* **46**, 1481–1492 (1998).
4. S. Ogata, J. Li, S. Yip, Energy landscape of deformation twinning in bcc and fcc metals. *Phys. Rev. B* **71**, 224102 (2005).
5. C. J. Healy, G. J. Ackland, Molecular dynamics simulations of compression–tension asymmetry in plasticity of Fe nanopillars. *Acta Mater.* **70**, 105–112 (2014).
6. A. S. Argon, S. R. Maloof, Plastic deformation of tungsten single crystals at low temperatures. *Acta Metall.* **14**, 1449–1462 (1966).
7. D. Caillard, Kinetics of dislocations in pure Fe. Part I. In situ straining experiments at room temperature. *Acta Mater.* **58**, 3493–3503 (2010).
8. C. R. Weinberger, W. Cai, Surface-controlled dislocation multiplication in metal micropillars. *Proc. Natl. Acad. Sci. U.S.A.* **105**, 14304–14307 (2008).
9. A. Paxton, P. Gumbsch, M. Methfessel, A quantum mechanical calculation of the theoretical strength of metals. *Philos. Mag. Lett.* **63**, 267–274 (1991).
10. S. I. Rao, C. Woodward, Atomistic simulations of (*a*/2)⟨111⟩ screw dislocations in bcc Mo using a modified generalized pseudopotential theory potential. *Philos. Mag. A* **81**, 1317–1327 (2001).
11. G. Wang, A. Strachan, T. Çağin, W. A. GoddardIII, Calculating the Peierls energy and Peierls stress from atomistic simulations of screw dislocation dynamics: Application to bcc tantalum. *Model. Simul. Mater. Sci. Eng.* **12**, S371–S389 (2004).
12. C. Woodward, S. I. Rao, *Ab-initio* simulation of isolated screw dislocations in bcc Mo and Ta. *Philos. Mag. A* **81**, 1305–1316 (2001).
13. C. Chisholm, H. Bei, M. B. Lowry, J. Oh, S. A. Syed Asif, O. L. Warren, Z. W. Shan, E. P. George, A. M. Minor, Dislocation starvation and exhaustion hardening in Mo alloy nanofibers. *Acta Mater.* **60**, 2258–2264 (2012).
14. J.-Y. Kim, D. Jang, J. R. Greer, Tensile and compressive behavior of tungsten, molybdenum, tantalum and niobium at the nanoscale. *Acta Mater.* **58**, 2355–2363 (2010).
15. J.-Y. Kim, D. Jang, J. R. Greer, Crystallographic orientation and size dependence of tension–compression asymmetry in molybdenum nano-pillars. *Int. J. Plast.* **28**, 46–52 (2012).
16. J. Wang, Z. Zeng, C. R. Weinberger, Z. Zhang, T. Zhu, S. X. Mao, *In situ* atomic-scale observation of twinning-dominated deformation in nanoscale body-centred cubic tungsten. *Nat. Mater.* **14**, 594–600 (2015).
17. A. S. Argon, S. R. Maloof, Fracture of tungsten single crystals at low temperatures. *Acta Metall.* **14**, 1463–1468 (1966).
18. J. W. Christian, S. Mahajan, Deformation twinning. *Prog. Mater. Sci.* **39**, 1–157 (1995).
19. Q. Wang, J. Wang, J. Li, Z. Zhang, S. X. Mao, Consecutive crystallographic reorientations and superplasticity in body-centered cubic niobium nanowires. *Sci. Adv.* **4**, eaas8850 (2018).
20. S. Wei, Q. Wang, H. Wei, J. Wang, Bending-induced deformation twinning in body-centered cubic tungsten nanowires. *Mater. Res. Lett.* **7**, 210–216 (2019).
21. G. Sainath, B. K. Choudhary, Orientation dependent deformation behaviour of BCC iron nanowires. *Comput. Mater. Sci.* **111**, 406–415 (2016).
22. S. Li, X. Ding, J. Deng, T. Lookman, J. Li, X. Ren, J. Sun, A. Saxena, Superelasticity in bcc nanowires by a reversible twinning mechanism. *Phys. Rev. B* **82**, 205435 (2010).
23. G. J. Ackland, R. Thetford, An improved *N*-body semi-empirical model for body-centred cubic transition metals. *Philos. Mag. A* **56**, 15–30 (1987).
24. D. Hull, D. J. Bacon, *Introduction to Dislocations* (Butterworth-Heinemann, 2001).
25. M.-C. Marinica, L. Ventelon, M. R. Gilbert, L. Proville, S. L. Dudarev, J. Marian, G. Bencteux, F. Willaime, Interatomic potentials for modelling radiation defects and dislocations in tungsten. *J. Phys. Condens. Matter* **25**, 395502 (2013).
26. D. Roundy, C. R. Krenn, M. L. Cohen, J. W. Morris Jr., The ideal strength of tungsten. *Philos. Mag. A* **81**, 1725–1747 (2001).
27. M. Černý, P. Šesták, J. Pokluda, Influence of superimposed normal stress on shear strength of perfect bcc crystals. *Comput. Mater. Sci.* **47**, 907–910 (2010).
28. M. Černý, P. Šesták, J. Pokluda, Strength of bcc crystals under combined shear and axial loading from first principles. *Comput. Mater. Sci.* **55**, 337–343 (2012).
29. G. Kresse, D. Joubert, From ultrasoft pseudopotentials to the projector augmented-wave method. *Phys. Rev. B* **59**, 1758 (1999).
30. J. P. Perdew, K. Burke, M. Ernzerhof, Generalized gradient approximation made simple. *Phys. Rev. Lett.* **77**, 3865–3868 (1996).
31. H. J. Monkhorst, J. D. Pack, Special points for Brillouin-zone integrations. *Phys. Rev. B* **13**, 5188 (1976).
32. A. Cao, Shape memory effects and pseudoelasticity in bcc metallic nanowires. *J. Appl. Phys.* **108**, 113531 (2010).
33. P. Wang, W. Chou, A. Nie, Y. Huang, H. Yao, H. Wang, Molecular dynamics simulation on deformation mechanisms in body-centered-cubic molybdenum nanowires. *J. Appl. Phys.* **110**, 093521 (2011).
34. Y. Lu, S. Xiang, L. Xiao, L. Wang, Q. Deng, Z. Zhang, X. Han, Dislocation "bubble-like-effect" and the ambient temperature super-plastic elongation of body-centred cubic single crystalline molybdenum. *Sci. Rep.* **6**, 22937 (2016).
35. H. Bei, S. Shim, G. M. Pharr, E. P. George, Effects of pre-strain on the compressive stress–strain response of Mo-alloy single-crystal micropillars. *Acta Mater.* **56**, 4762–4770 (2008).
36. S. M. Han, T. Bozorg-Grayeli, J. R. Groves, W. D. Nix, Size effects on strength and plasticity of vanadium nanopillars. *Scr. Mater.* **63**, 1153–1156 (2010).
37. A. B. Hagen, B. D. Snartland, C. Thaulow, Temperature and orientation effects on the deformation mechanisms of α-Fe micropillars. *Acta Mater.* **129**, 398–407 (2017).
38. B. R. S. Rogne, C. Thaulow, Strengthening mechanisms of iron micropillars. *Philos. Mag.* **95**, 1814–1828 (2015).
39. K. Y. Xie, Y. Wang, S. Ni, X. Liao, J. M. Cairney, S. P. Ringer, Insight into the deformation mechanisms of α-Fe at the nanoscale. *Scr. Mater.* **65**, 1037–1040 (2011).
40. B. R. S. Rogne, C. Thaulow, Effect of crystal orientation on the strengthening of iron micro pillars. *Mater. Sci. Eng. A* **621**, 133–142 (2015).



#### Acknowledgments

**Funding:** J.W. acknowledges support from the National Natural Science Foundation of China (nos. 51701179 and 51771172) and the Innovation Fund of the Zhejiang Kechuang New Materials Research Institute (no. ZKN-18-Z02). T.Z. acknowledges support from the U.S. National Science Foundation (grant DMR-1410331). H.T. acknowledges support from the National Natural Science Foundation of China (no. 11725210). **Author contributions:** J.W. and

T.Z. conceived the idea and designed the project. J.W. and Q.W. conducted the experiments and analyzed the data. Z.Ze., M.W., D.C., Y.Z., P.W., and T.Z. performed the simulations. H.W., S.X.M., and Z.Zh. contributed to discussion. J.W. and T.Z. wrote and revised the paper. **Competing interests:** The authors declare that they have no competing interests. **Data and materials availability:** All data needed to evaluate the conclusions in the paper are present in the paper and/or the Supplementary Materials. Additional data related to this paper may be requested from the authors.

Submitted 8 June 2019
Accepted 8 April 2020
Published 3 June 2020
10.1126/sciadv.aay2792

**Citation:** J. Wang, Z. Zeng, M. Wen, Q. Wang, D. Chen, Y. Zhang, P. Wang, H. Wang, Z. Zhang, S. X. Mao, T. Zhu, Anti-twinning in nanoscale tungsten. *Sci. Adv.* **6**, eaay2792 (2020).